PHOTONICS Research

Wide-field ophthalmic space-division multiplexing optical coherence tomography

Jason Jerwick,[1,2] Yongyang Huang,[1] Zhao Dong,[1,2] Adrienne Slaudades,[3] Alexander J. Brucker,[3] and Chao Zhou[1,2,4,*]

[1]Department of Electrical and Computer Engineering, Lehigh University, Bethlehem, Pennsylvania 18015, USA
[2]Department of Biomedical Engineering, Washington University in St. Louis, St. Louis, Missouri 63130, USA
[3]Scheie Eye Institute, Penn Presbyterian Medical Center, University of Pennsylvania, Philadelphia, Pennsylvania 19104, USA
[4]Department of Bioengineering, Lehigh University, Bethlehem, Pennsylvania 18015, USA
*Corresponding author: chaozhou@wustl.edu

Received 13 November 2019; revised 16 January 2020; accepted 17 January 2020; posted 23 January 2020 (Doc. ID 383034); published 31 March 2020

High-speed ophthalmic optical coherence tomography (OCT) systems are of interest because they allow rapid, motion-free, and wide-field retinal imaging. Space-division multiplexing optical coherence tomography (SDM-OCT) is a high-speed imaging technology that takes advantage of the long coherence length of microelectromechanical vertical cavity surface emitting laser sources to multiplex multiple images along a single imaging depth. We demonstrate wide-field retinal OCT imaging, acquired at an effective A-scan rate of 800,000 A-scans/s with volumetric images covering up to 12.5 mm × 7.4 mm on the retina and captured in less than 1 s. A clinical feasibility study was conducted to compare the ophthalmic SDM-OCT with commercial OCT systems, illustrating the high-speed capability of SDM-OCT in a clinical setting.

https://doi.org/10.1364/PRJ.383034

1. INTRODUCTION

Since its inception in 1991, optical coherence tomography (OCT) has revolutionized diagnostic care for retinal diseases [1,2]. The ability to resolve high-resolution cross-sectional and volumetric images of the macula has been key for diagnosis of retina diseases like age-related macular degeneration, macular edema, diabetic retinopathy, and retinitis pigmentosa [3–7]. Due to imaging speed limitations, volumetric imaging has historically been limited to the macula region of the retina. This region contains most of a patient's central vision, making it the most important region to detect retinal abnormalities. Recently, there has been increased interest in high-resolution imaging of the regions outside of the macula, the retina periphery [8,9]. Retinal disease may originate in regions outside of the macula and may progress for years unnoticed to the patient and without loss of central vision. With high-resolution wide-field imaging, these early stage disease progressions can be detected, and preventative treatment can be commenced. This strategy could stop vision deterioration before the patient loses any central vision, greatly reducing morbidity.

One of the key image quality problems in ophthalmic OCT is motion artifacts [10,11]. Many ophthalmic patients are elderly and have the inability to sit still for more than a few seconds. Additional sources of motion artifacts include involuntary micro saccades and even the patient's breaths and heartbeats. To reduce the probability of motion artifacts, ophthalmic OCT images must be acquired rapidly, or motion tracking hardware and software must be employed [12]. Typical OCT eye-tracking systems employ a scanning laser ophthalmoscope (SLO) to produce *en face* images of the retina that the OCT scans can be registered against [13]. This increases system complexity and may not have high enough registration performance to acquire accurate volumetric scans [14]. Most commercial OCT systems are limited by scan speeds of tens of kilohertz. Due to the large number of A-scans required and extended scan periods, OCT volume scans with commercial systems are often untenable, even over small scan ranges. Many commercial systems use a range of scan patterns, including tens of B-scans over small scan ranges (up to 6 mm × 6 mm), denser cube scans with up to 100 B-scans (3 mm × 3 mm), and single B-scans over wider ranges (10 mm × 0 mm). An order of magnitude imaging speed increase is necessary to produce motion-artifact-free, high-resolution, high sampling density, and volumetric and wide-field retinal imaging.

Because this is an important problem, the development of high-speed OCT systems has been an active area of research [14–17]. Most commercial OCT systems are spectral domain, which are limited by the spectrometer camera frame rate. During the last 10 years, there has been increased focus on the development of swept-source OCT (SS-OCT), which is limited by the sweep rate of the laser source.

Microelectromechanical vertical cavity surface emitting laser (MEMs VCSEL) sources can be implemented at 50–580 kHz, and Fourier domain mode locking (FDML) sources have been demonstrated in excess of 3 MHz [15–18]. Additionally, high-speed line-field and full-field SS-OCT systems have been demonstrated [19,20]. These ultra-high-speed megahertz systems are capable of rapid volume acquisition, but they do suffer some limitations. The most pressing limitation is the reduced sensitivity in these systems due to the reduced exposure time at each sample point. In the 1060 nm wavelength region, typically used in high-speed retinal imaging, illumination power is limited to 1.8 mW by the American National Standards Institute (ANSI) safety standard. This power limitation limits the sensitivity of megahertz systems to less than 90 dB [14,21]. Images acquired with sensitivities below 90 dB have poor image quality without extensive averaging. Some megahertz systems use up to 96× averaging to achieve reasonable image quality, which increases the overall scan time significantly [14]. Additionally, ultra-high-speed systems require the galvanometer scanner to be driven at high frequencies, which can warp the image or damage the galvanometer. Resonant scanners may be required.

Space-division multiplexing optical coherence tomography (SDM-OCT) is a high-speed OCT system that takes advantage of the long coherence length of VCSELs to multiplex multiple images along the imaging depth [22]. This parallel imaging technique splits the sample arm light into multiple channels and imparts an optical path length delay to each channel. Each of these imaging channels illuminates a different position on the sample, enabling simultaneous imaging of multiple locations, increasing the effective image speed. VCSELs can have coherence lengths on the order of centimeters, whereas the penetration depth of near-infrared (NIR) OCT imaging light is typically less than 2 mm [23]. This mismatch between laser coherence length and imaging penetration depth means that the total amount of information that the interference fringe can carry is not being fully utilized with the use of a single imaging beam. By adding optical path length delays longer than the optical penetration depth in tissue to the parallel channels, parallel images can be acquired simultaneously without overlapping. The advantage of SDM-OCT is that the multiple imaging beams can be acquired by a single detector, which has reduced system complexity compared to other multi-beam OCT systems [24–28]. Previous implementations of SDM-OCT have used both fiber-based splitters and silicon-on-insulator (SOI) photonic chips to generate eight parallel imaging channels [22,29]. Also, previous systems have operated at 1310 nm wavelengths. The 1310 nm wavelength range is not suitable for ophthalmic imaging due to the strong absorption of water in this region and the necessity to penetrate through >2 cm of vitreous humor to reach the retina. The 1060 nm light has up to 100× lower absorption in water than 1310 nm light. In this study, we develop a four-beam 1060 nm SDM-OCT system for wide-field ophthalmic applications. Table 1 shows a comparison of published SDM-OCT systems.

2. METHODS

A. System Description

The system source is a 1060 nm MEMs VCSEL swept-source operating at 200 kHz. This source has an output power of 35 mW and a −15 dB bandwidth of 104 nm (Thorlabs). The source light was further amplified by a booster optical amplifier (BOA) to achieve a system input power of 55 mW, enough power for the Mach–Zehnder interferometer (MZI), reference arm, and all four sample beams. The system topology is shown in Fig. 1. After the BOA, 5% of the light is split to an MZI to produce a parallel calibration signal. From here, the light is split 95:5 again, with 5% going to a single-pass reference arm and 95% to the sample arm. The sample arm is then split 80:20, with 20% continuing to a custom 1×4 SDM fiber splitter and 80% of the light lost. After traveling through the sample arm optics, backscattered light returns through the 1×4 SDM splitter and interferes with light from the single-pass reference arm. The interference signal is detected by a balanced photodetector (Thorlabs PBD481c). The OCT and MZI interference signals are captured in parallel by a high-speed digitizer (Alazar Tech ATS9373) operating at 1.5 GHz. System imaging range is 12.5 mm in air at this sampling frequency. The system design is constrained by the inherent back coupling losses to SDM-OCT. The sample arm is split into four beams that cause 6 dB of inherent back coupling losses. At the high operating speed of the system, every effort must be made to conserve as much sensitivity as possible. To minimize further losses, an 80:20 splitter is used to couple the backscattered light to the detection arm. This saves 80% of backscattered light as opposed to 50% with a 50:50 splitter. This results in a sensitivity gain of ∼2 dB with power on the sample conserved. The 80:20 splitter also has lower back coupling loss and broader bandwidth performance than available circulators. The cost of this design is that 80% of the input power is lost, requiring high laser power and optical amplification. A narrowband fiber Bragg grating (FBG) ($\Delta\lambda = 0.4$ nm, $\lambda_0 = 1020$ nm, O/E Land) is inserted into one arm of the MZI for accurate fringe jitter registration. This increases the phase stability and ensures the axial resolution within the deeper beams is maintained [30]. In the reference arm, four lenses, matching the lenses in the sample arm, were used to match dispersion. Additionally, dispersion-compensating

Table 1. Comparison of SDM-OCT Systems

System	Center Wavelength (nm)	Laser Sweep Rate (kHz)	Beams	Effective A-Scan Rate (kHz)	Sensitivity (dB)
1st generation SDM-OCT [22]	1310	100	8	800	94.6
SOI chip-based SDM-OCT [29]	1310	100	8	800	91
Ophthalmic SDM-OCT	1060	200	4	800	91

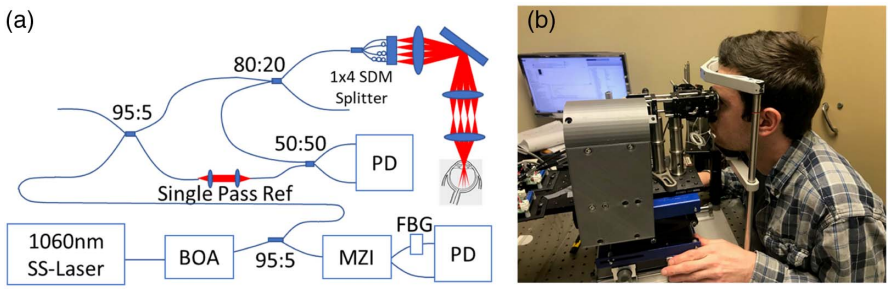

Fig. 1. (a) Schematic for the ophthalmic SDM-OCT system. BOA, booster optical amplifier; FBG, fiber Bragg grating; MZI, Mach–Zehnder interferometer; PD, balanced photodetector. (b) Picture of the ophthalmic SDM-OCT prototype in the clinic.

glasses were inserted into the reference arm to compensate for dispersion in the ophthalmic lens. Numerical dispersion compensation was used to compensate for dispersion in the vitreous humor and for dispersion fine-tuning [31].

1. Safety Considerations

The ophthalmic SDM-OCT system was approved for human imaging by institutional review boards (IRBs) at both Lehigh University and University of Pennsylvania. The ANSI standard prescribes the maximum power incident on the eye for a 1060 nm single laser source as 1.8 mW [32]. This system utilizes <1.8 mW per imaging beam, resulting in a total incident power on the eye of <7.2 mW, seemingly higher than the ANSI standard. The ANSI standard declares that in the case of multiple sources, their optical powers may be considered separately if the angle of incidence on the eye between the sources is >100 mrad [32]. Because the four beams used in the SDM-OCT system are separated by more than 100 mrad, we can consider them separately. All four beams intersect at the scan pivot point, which is near the cornea. This increases the power density at the cornea by 4 times. Still, the irradiance on the cornea is quite low, ~14 $\mathrm{mW/cm^2}$, because the beams are collimated at this point. Also, the absorption of NIR light in corneal tissue is many times less efficient than in retinal tissue. Due to the optical power of the eye, the irradiance on the retina is typically 2×10^5 higher than that on the cornea. This indicates that even with multiple beams entering the cornea, the irradiance at the cornea will be 4 orders of magnitude smaller than the irradiance at each spot on the retina. The lower irradiance, in combination with the increased translucence of the cornea over the retina, means that the risk of acute corneal damage is very low. The irradiance of this device on the cornea is similar to NIR irradiance in ambient daylight (1–10 $\mathrm{mW/cm^2}$), and studies have shown that incidental exposures of up to 100 $\mathrm{mW/cm^2}$ are acceptable for several minutes [33]. Therefore, SDM-OCT presents minimal risk to patients.

2. Sample Arm Optics Design

Choosing an appropriate interbeam optical path distance is important because we must consider the penetration depth of a single beam, the curvature of the eye, and the system imaging range. Also, the lateral displacement of the imaging beams is important to satisfy the ANSI standard for distributed sources. The fiber tips are laterally spaced by 500 μm on the custom 1×4 SDM splitter (AC Photonics) to provide each imaging beam with sufficient displacement on the eye. The 3 mm fiber length difference between each channel provides optical delays necessary to prevent overlapping between adjacent imaging channels. By choosing a beam path length difference of 3 mm, all four beams do not overlap over a broad scan range of 60 deg and fit into the imaging depth range of 12.5 mm. The four imaging beams are relayed to the eye via three lenses. The beams are collimated by an $f_1 = 30$ mm lens, focused by an $f_2 = 50$ mm lens, and then collimated again with a wide-field ophthalmic lens to ensure proper focus on the retina. This results in an estimated lateral displacement between beams on the retina of ~1.85 mm, corresponding to an angular separation of ~100 mrad. Because of the fixed nature of the fiber-based splitter, the imaging range without overlap between beams along this dimension is fixed at 7 mm. This reduces the flexibility of the system somewhat. A dichroic mirror was used to focus an illuminated green cross onto the eye for use as a fixation target for the patient. The sample arm was fixed to a retrofitted slit lamp base so patients could be comfortably imaged with the system [Fig. 1(b)].

The theoretical sensitivity of a single-beam OCT system operating at 200 kHz with a 68% duty cycle, 1.8 mW power on the sample, and 0.7 detector sensitivity is ~100.4 dB [Eq. (1)] [21]. Accounting for the 6 dB loss from the 1×4 splitter and the 1 dB loss from the 80:20 splitter brings the theoretical sensitivity of our SDM-OCT system to ~93.4 dB. Measured sensitivity of this system was ~91 dB, indicating ~2.4 dB in additional optical losses. System axial resolution is measured to be ~6.8 μm in tissue with an axial pixel size of ~4.3 μm:

$$\mathrm{SNR}_{\mathrm{ssoct}} = \frac{\rho S R_s \Delta t}{2e}. \tag{1}$$

B. Image Processing

SDM-OCT fringes were acquired in parallel with MZI calibration fringes. Every SDM-OCT A-scan fringe was registered to the FBG peak and interpolated based on the MZI calibration fringe. SDM-OCT frames were discrete Fourier transform registered to reduce axial motion artifacts [34]. The four SDM-OCT beams were manually stitched using ImageJ. A mean filter was applied to reduce speckle noise. Stitched SDM-OCT images were flattened by segmenting the retinal pigment epithelium (RPE) with a graph cut segmentation technique [35]. Cross-sectional images and *en face* projections were

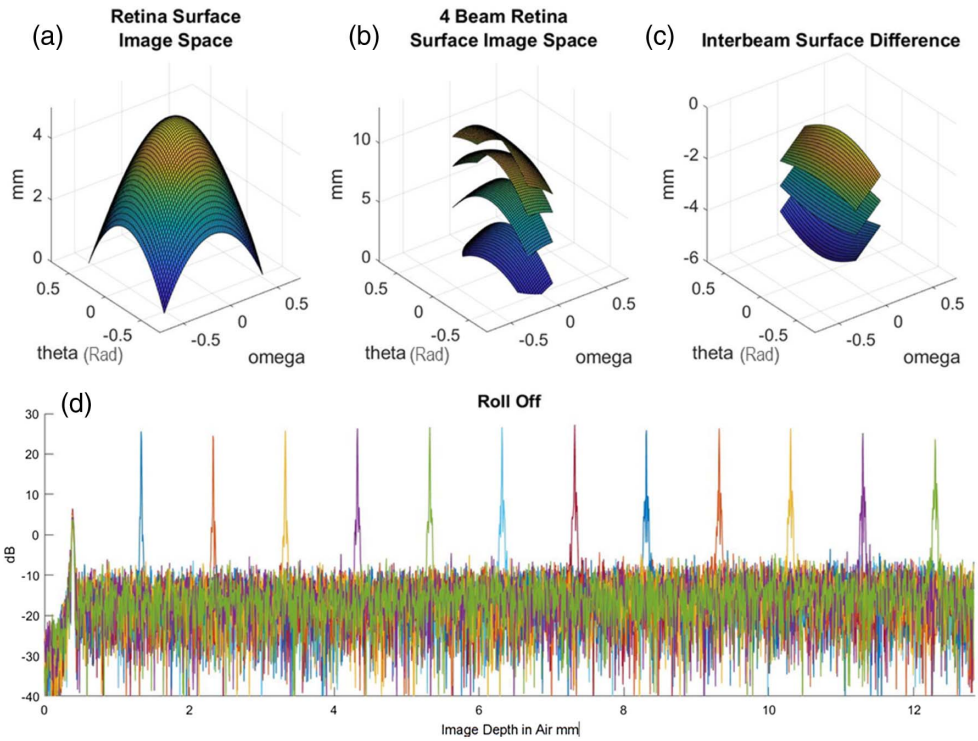

Fig. 2. Geometric considerations for ophthalmic SDM-OCT design. (a) Projection of the curvature of the eye onto the imaging space. (b) Image space separated into four imaging beams with 3 mm optical delay. All four beams fit in the 12 mm image depth. (c) Distance between adjacent beams shows there is no overlapping between adjacent images. (d) Sensitivity roll-off measured over the entire imaging depth range.

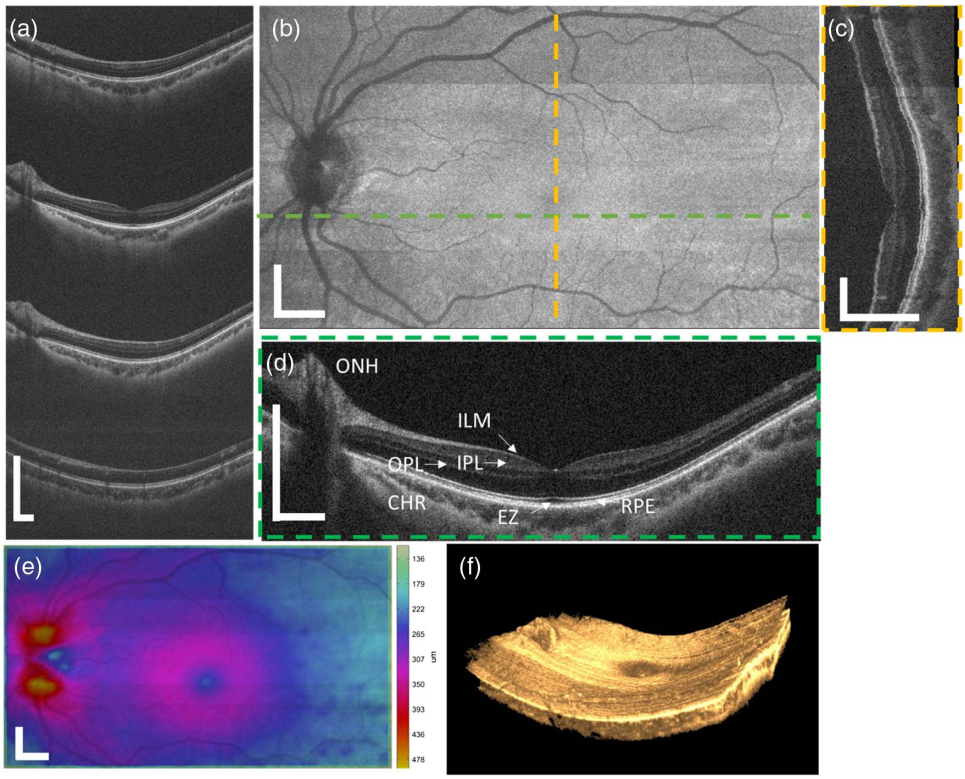

Fig. 3. (a) Four-beam raw SDM-OCT image. (b) *En face* projection of the RPE layer; yellow line shows location of vertical cross section and green line shows location of horizontal cross-section. (c) Vertical cross-section. (d) Horizontal cross-section with some selected anatomical features labeled. CHR, choroid; EZ, ellipsoid zone; ILM, internal limiting membrane; IPL, inner plexiform layer; ONH, optic nerve head; OPL, outer plexiform layer; RPE, retinal pigment epithelium. (e) Retinal thickness map. (f) 3D rendering of stitched SDM-OCT images (also see Visualization 1). Scale bars 1 mm.

extracted from the flattened image. Retina thickness maps were generated by segmentation of internal limiting membrane (ILM) and the RPE. The axial positions of the ILM and RPE were subtracted for each frame to calculate the two-dimensional (2D) retinal thickness. For visualization, retinal thickness was mapped to hue and projected onto an *en face* projection of the RPE.

C. Clinical Feasibility Study

A clinical feasibility study was conducted at Scheie Eye Institute at the University of Pennsylvania. Ten patients between the ages of 18 and 80 with previous diagnosis of retinal disease were recruited. SDM-OCT images were acquired for both of each patient's eyes. Reference OCT images were acquired with commercial OCT systems (Heidelberg Spectralis or Zeiss Cirrus).

3. RESULTS

A. System Characterization

To design the optical path length difference between each of the SDM-OCT channels, the curvature of the retina must be taken into account to prevent image overlapping. Figure 2 shows the projection of the curvature of the eye onto the SDM-OCT image space as calculated by the eye scan model introduced by Kolb *et al.* [16]. Equation (2) shows how the curvature of the image space was calculated, with r being the radius of the eye, d' the depth of the scan pivot point, and ε the scan angle [16]:

$$\mathrm{iOPD} = n \cdot [(2 - \cos\varepsilon)r - (1 - \cos\varepsilon)d' - \sqrt{r^2 - (r - d')^2 \sin^2\varepsilon}]. \quad (2)$$

Figure 2(a) shows how the surface of the retina is curved in the image space over a scan range of 0.5 rad. By splitting this space into four imaging "strips" [Fig. 2(b)] with spatial offsets, we can simulate the shape of the wide-field retinal SDM-OCT image. Calculating the z distance between each of these retinal surfaces [Fig. 2(c)] ensures that there is sufficient space between beams to prevent overlapping over the total scan range. The 3 mm of optical path length difference (OPD) between the channels was sufficient to prevent interbeam image overlapping. To ensure image quality was maintained over all four beams, the sensitivity roll-off was measured over the entire imaging range. A 3 dB sensitivity roll-off over 12.5 mm was measured [Fig. 2(d)]. Beam power was measured after the second lens in the sample arm. Power was measured to be 1.60, 1.78, 1.70, and 1.63 mW for beams 1, 2, 3, and 4, respectively.

B. Tests on Healthy Subjects

Initial tests were conducted on healthy volunteers. The capabilities of ophthalmic SDM-OCT are illustrated in Fig. 3. Figure 3(a) shows a typical raw ophthalmic SDM-OCT image with the image zero crossing at the top of the image. There are no overlaps between adjacent imaging beams and no cross talk between channels. A single B-scan is 2250 pixels deep by

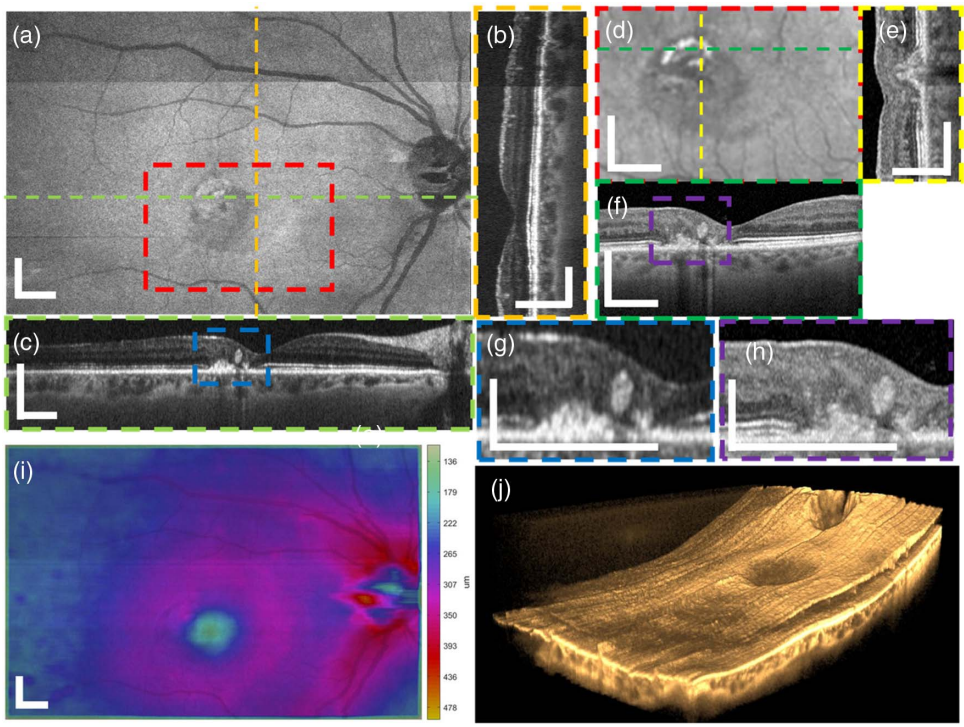

Fig. 4. SDM-OCT and commercial OCT images from a patient diagnosed with retinal telangiectasia. (a) *En face* projection SDM-OCT. (b) Vertical cross-section SDM-OCT. (c) Horizontal cross-section SDM-OCT. (d) *En face* SLO image of commercial system imaging range (5 mm × 3 mm). (e) Vertical cross-section commercial OCT. (f) Horizontal cross-section commercial OCT. (g) Zoomed-in region of interest (ROI) from SDM-OCT. (h) Zoomed-in ROI from commercial OCT. (i) Retinal thickness map. (j) 3D rendering of stitched SDM-OCT images (also see Visualization 2). Lateral scale bars 1 mm. Axial scale bars 500 μm for (b), (c), (e), and (f) and 200 μm for (g) and (h).

1000 pixels wide. The wide-field capabilities are illustrated in Figs. 3(b)–3(e). The *en face* projection of the RPE layer of the retina in Fig. 3(b) provides a clear illustration of image range capabilities of this system, whereas Figs. 3(c) and 3(d) demonstrate that this system is capable of producing high-density cross sections across both the horizontal and vertical dimensions. The sub 1 s acquisition time allows this large volumetric acquisition to be implemented free of motion artifacts. A wide-field retina thickness map is shown in Fig. 3(e). A volumetric rendering of the 12.5 mm × 7.4 mm imaging region is shown in Fig. 3(f) with 600,000 total effective A-scans. Visualization 1 shows the B-scan stack from the same SDM-OCT three-dimensional (3D) dataset. Intensity differences are visible between each of the imaging beams, with images 1 and 4 having lower intensity. This is due to power nonuniformity between the beams and focus differences on the retina.

C. Clinical Feasibility Study

A clinical feasibility study was conducted at the University of Pennsylvania's Scheie Eye Institute. SDM-OCT and commercial OCT images were acquired from 10 patients with various diagnosed retinal pathologies. Comparisons between SDM-OCT and commercial OCT images from patients are shown in Figs. 4 and 5. Figure 4 contains images from the right eye of a patient diagnosed with retinal telangiectasia. Retinal telangiectasia is a rare retinal disorder characterized by abnormalities in macular vascular structure and growth of neovascular membranes in the ellipsoid zone [36]. From the wide-field *en face* view of the SDM-OCT images, a large disturbance can be seen in the RPE around the macula [Fig. 4(a)]. Figures 4(b) and 4(c) show wide-field vertical and horizontal cross sections from the SDM-OCT volume image, respectively. The shape and structure of this abnormality match well with the 5 mm × 3 mm *en face* SLO image in Fig. 4(d). The red box in Fig. 4(a) represents the scan range of the commercial OCT system. Figures 4(e) and 4(f) show the corresponding vertical and horizontal cross sections acquired with the commercial system. This dense scan consisted of 1024 A-scans × 96 B-scans. The axial resolution of this commercial system is ~3.9 μm. Figures 4(g) and 4(h) are zoomed-in comparisons of a region of the macula presenting pathology. Features match well between the SDM-OCT image [Fig. 4(g)] and the commercial OCT image [Fig. 4(h)]. The resolution of the SDM-OCT is lower because of the lower axial resolution of 1060 nm OCT compared to 800 nm OCT and the filtering used to remove speckle noise from the image. Figures 4(i) and 4(j) show the retinal thickness map and 3D rendering, respectively. The corresponding volumetric SDM-OCT image stack is shown in Visualization 2.

A second example is shown in Fig. 5. This patient was diagnosed with exudative age-related macular degeneration.

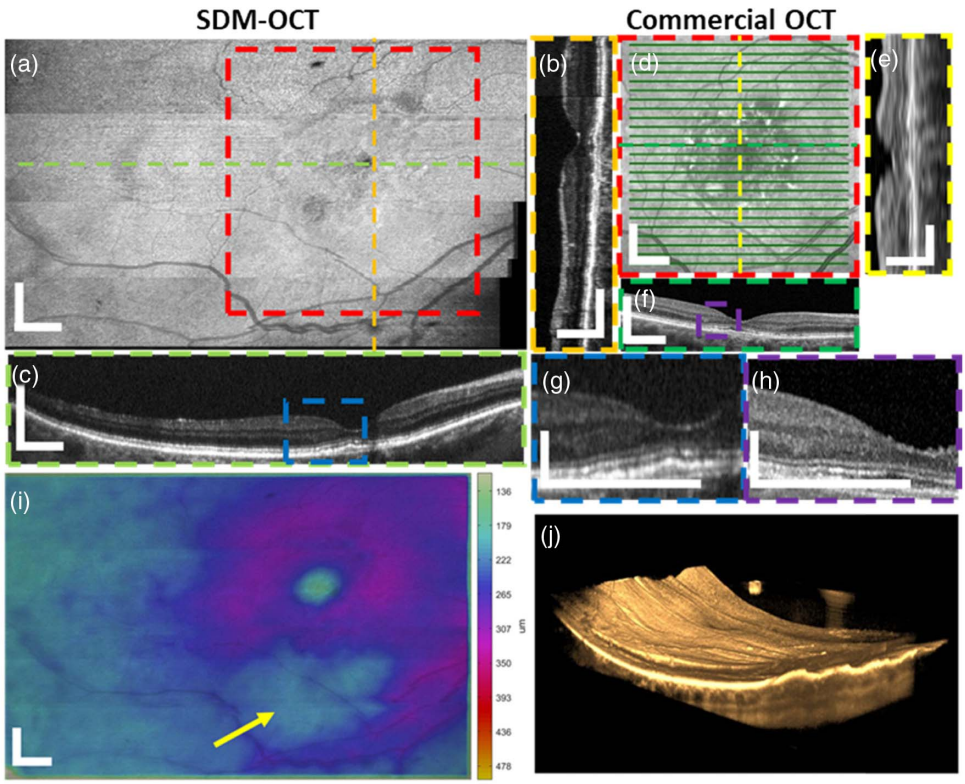

Fig. 5. SDM-OCT and commercial OCT images from a patient diagnosed with exudative age-related macular degeneration. (a) *En face* projection of RPE SDM-OCT. (b) Vertical cross-section SDM-OCT. (c) Horizontal cross-section SDM-OCT. (d) *En face* SLO image of commercial system imaging range. (e) Vertical cross-section commercial OCT. (f) Horizontal cross-section commercial OCT. (g) Zoomed-in ROI from SDM-OCT. (h) Zoomed-in ROI from commercial OCT. (i) Retinal thickness map. Yellow arrow indicates region with retinal thinning. (j) 3D rendering of stitched SDM-OCT images (also see Visualization 3). Lateral scale bars 1 mm. Axial scale bars 500 μm for (b), (c), (e), and (f) and 200 μm for (g) and (h).

Figures 5(a)–5(c) show the *en face*, vertical, and horizontal cross sections of the SDM-OCT image, respectively. The images from the commercial OCT system [Figs. 5(d)–5(f)] were acquired with a typical low-density B-scan scan pattern. Here only 18 loosely spaced B-scans are acquired. This is a common scan pattern because it can be acquired rapidly with the low acquisition speed of the commercial SD-OCT system (40 kHz A-scan rate). This limits the resolution of vertical cross sections immensely as can be seen in Fig. 5(e). Once again, a region of the macula is selected to compare the image quality of the SDM-OCT and commercial OCT systems. An interruption in the RPE layer is clearly visible in both images. A wide-field thickness map of the retina [Fig. 5(i)], generated from the SDM-OCT image, shows substantial retinal thinning in the outer region of the retina. Figure 5(j) shows the 3D rendering of the SDM-OCT images (volumetric videos shown in Visualization 3).

Another patient was diagnosed with non-proliferative diabetic retinopathy in his left eye. A similar comparison between SDM-OCT and commercial OCT images is made in Fig. 6. In this case, the wide-field volumetric capabilities of SDM-OCT prove especially useful. *En face*, vertical, and horizontal cross sections of the SDM-OCT image are shown in Figs. 6(a)–6(c). With the small scan range and low B-scan density of the commercial OCT system [Figs. 6(d)–6(f)], the OCT findings were found to be normal based on the interpretation of an expert physician, but when the SDM-OCT image is viewed in the *en face* plane, some abnormalities become apparent. Figure 6(i) shows an *en face* projection of the SDM-OCT image through the OPL layer of the retina. In the periphery of this *en face* projection, many small, bright scatterers can be seen (yellow arrows). An experienced ophthalmologist determined that these scatterers are likely microcysts or microaneurysms. Figure 6(j) shows a fluorescein angiogram acquired from the same eye during a visit 2 months before the SDM-OCT images were acquired. A pattern of matching microcysts can be seen, indicated by the yellow arrows. The *en face* SDM-OCT was also compared with a red free fundus image (not shown), which further supported that these spots were microcysts. The narrow range and low scan density of the standard OCT scan missed all of the bright spots, which could have resulted in missed diagnosis. This clearly demonstrates the importance of wide-field

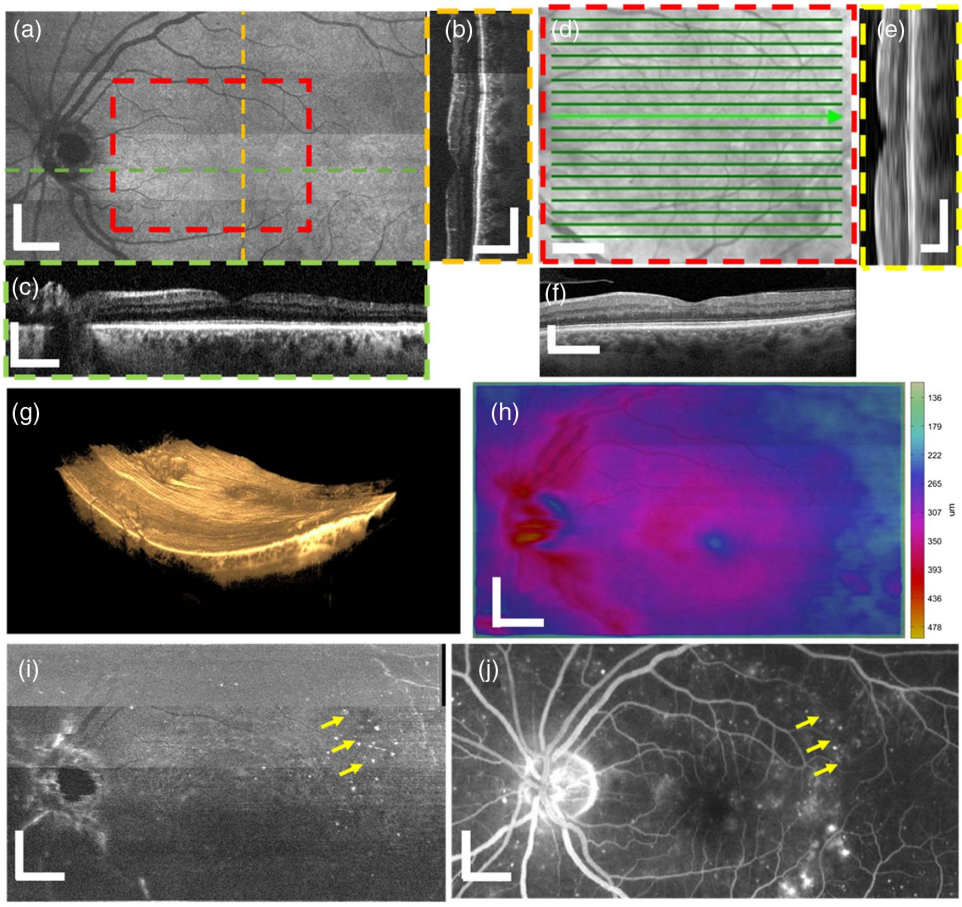

Fig. 6. SDM-OCT and commercial OCT images from a patient diagnosed with non-proliferative diabetic retinopathy. (a) *En face* projection SDM-OCT. (b) Vertical cross-section SDM-OCT. (c) Horizontal cross-section SDM-OCT. (d) *En face* SLO image of commercial system imaging range. (e) Vertical cross-section commercial OCT. (f) Horizontal cross-section commercial OCT. (g) 3D rendering of SDM-OCT image stack (also see Visualization 4). (h) Retinal thickness map. (i) *En face* projection of the outer plexiform layer showing microcysts highlighted by the yellow arrows. (j) Fluorescein angiogram showing matching microcysts to Fig. 5(h). Lateral scale bars 1 mm. Axial scale bars 500 μm for (b), (c), (e), and (f).

imaging. The 3D rendering and retinal thickness map are shown in Figs. 6(g) and 6(h), respectively. Cross-sectional SDM-OCT images are shown in Visualization 4.

4. DISCUSSION

The SDM-OCT system we demonstrated here utilizes a parallel imaging approach to acquire volumetric retinal images at speeds >10× faster than commercial SD-OCT systems and 4× faster that MEMs VCSEL-based single-beam SS-OCT systems. Higher OCT imaging speeds have been achieved with FDML lasers [14,16], but SDM-OCT has some advantages over these methods. First, the parallel imaging approach means that each B-scan acquisition is acquired at a much slower rate than for an equivalent single-beam system. This allows us to use a traditional galvanometer with a sawtooth waveform with minimal distortion. Megahertz OCT systems often require B-scans to be acquired in excess of 1000 Hz, which may necessitate the use of resonant scanners and sine waveforms.

The clinical feasibility study conducted here showed good matching between pathological features seen in SDM-OCT images and commercial OCT images. We were able to acquire wide-field structural images in less than 1 s. These wide-field volumetric images had high resolution over an imaging range of 12.5 mm × 7.4 mm, enabling simultaneous imaging of the optic nerve head and macula with minimal motion artifacts. We showed the importance of wide-field imaging by illustrating a case where pathology was missed within a standard OCT scan but was obvious under wide-field volumetric imaging (Fig. 6).

Although SDM-OCT offers key advantages in imaging speed, there are some limitations. The biggest drawback of this method at this stage is the relatively low imaging sensitivity, which results in more-noisy images and requires extensive filtering to improve image contrast. This system has a sensitivity of 91 dB, whereas commercial OCT systems typically operate with sensitivities greater than 100 dB. This low sensitivity is principally caused by the 6 dB backpropagation loss through the 1 × 4 fiber splitter in conjunction with the already limited sensitivity of the 200 kHz swept-source engine on which this method is based. It is important to note that sensitivity of this system, which operates at 800,000 effective A-scans/s, is theoretically identical to an equivalent single-beam OCT system with a true A-scan rate of 800,000 A-scans/s. We are working to develop topologies that avoid some of this backpropagation loss. The current low sensitivity limits the phase stability of the system and degrades the quality of functional measurement like Doppler OCT and angiography.

One another limitation of this method is the limited flexibility of the scan patterns that can be used with this method. The scan range along the vertical direction is fixed due to the fixed separation distance of the parallel imaging beams. Changing the distance between beams is possible with changes to sample arm optics, but the minimum distance between beams is limited by the ANSI definition of distributed sources. Beams that are closer than this limit increase the risk of thermal injury to the retina. This limits the ability to perform small-range, high-resolution, high-density scan patterns that are comparable to commercial OCT macula scan patterns. Additional limitations include the beam power nonuniformity, which can cause differences in image brightness between imaging beams and the necessity to stitch the four parallel images together, which can be a time-consuming process if done manually.

5. CONCLUSION

We demonstrate an ophthalmic SDM-OCT system, which can acquire retinal depth sections at an equivalent A-scan rate of 800 kHz. This allows rapid acquisition of volumetric, wide-field retina images for the diagnosis of retina diseases. A clinical feasibility study was conducted to analyze the image quality of the ophthalmic SDM-OCT prototype and make comparisons between SDM-OCT images and commercial OCT images. These high-speed, wide-field SDM-OCT acquisitions may reduce motion artifacts and prevent missed diagnosis of peripheral retinal disease.

Funding. National Science Foundation (DBI-1455613, IIP-1623823, IIP-1640707); National Institutes of Health (R01-EB025209).

Acknowledgment. The authors would like to thank Mrs. Joan Dupont and Dr. Benjamin Kim for their assistance in the recruitment of patients in this study.

Disclosures. The authors declare no conflicts of interest related to this paper.

REFERENCES

1. D. Huang, E. A. Swanson, C. P. Lin, J. S. Schuman, W. G. Stinson, W. Chang, M. R. Hee, T. Flotte, K. Gregory, and C. A. Puliafito, "Optical coherence tomography," Science **254**, 1178–1181 (1991).
2. J. Fujimoto and E. Swanson, "The development, commercialization, and impact of optical coherence tomography," Invest. Ophthalmol. Vis. Sci. **57**, OCT1–OCT13 (2016).
3. L. M. Sakata, J. DeLeon-Ortega, V. Sakata, and C. A. Girkin, "Optical coherence tomography of the retina and optic nerve—a review," Clin. Exp. Ophthalmol. **37**, 90–99 (2009).
4. M. R. Hee, C. R. Baumal, C. A. Puliafito, J. S. Duker, E. Reichel, J. R. Wilkins, J. G. Coker, J. S. Schuman, E. A. Swanson, and J. G. Fujimoto, "Optical coherence tomography of age-related macular degeneration and choroidal neovascularization," Ophthalmology **103**, 1260–1270 (1996).
5. M. R. Hee, C. A. Puliafito, C. Wong, J. S. Duker, E. Reichel, B. Rutledge, J. S. Schuman, E. A. Swanson, and J. G. Fujimoto, "Quantitative assessment of macular edema with optical coherence tomography," JAMA Ophthalmol. **113**, 1019–1029 (1995).
6. A. Ishibazawa, T. Nagaoka, A. Takahashi, T. Omae, T. Tani, K. Sogawa, H. Yokota, and A. Yoshida, "Optical coherence tomography angiography in diabetic retinopathy: a prospective pilot study," Am. J. Ophthalmol. **160**, 35–44 (2015).
7. H. Hirakawa, H. Iijima, T. Gohdo, and S. Tsukahara, "Optical coherence tomography of cystoid macular edema associated with retinitis pigmentosa," Am. J. Ophthalmol. **128**, 185–191 (1999).
8. A. Nagiel, R. A. Lalane, S. R. Sadda, and S. D. Schwartz, "Ultra-wide-field fundus imaging: a review of clinical applications and future trends," Retina **36**, 660–678 (2016).
9. V. Manjunath, V. Papastavrou, D. H. W. Steel, G. Menon, R. Taylor, T. Peto, and J. Talks, "Wide-field imaging and OCT vs clinical evaluation of patients referred from diabetic retinopathy screening," Eye **29**, 416 (2015).
10. E. A. T. Say, S. Ferenczy, G. N. Magrath, W. A. Samara, C. T. L. Khoo, and C. L. Shields, "Image quality and artifacts on optical coherence tomography angiography: comparison of pathologic and paired fellow

eyes in 65 patients with unilateral choroidal melanoma treated with plaque radiotherapy," Retina **37**, 1660–1673 (2017).
11. S. H. Yun, G. J. Tearney, J. F. de Boer, and B. E. Bouma, "Motion artifacts in optical coherence tomography with frequency-domain ranging," Opt. Express **12**, 2977–2998 (2004).
12. R. F. Spaide, J. G. Fujimoto, and N. K. Waheed, "Image artifacts in optical coherence tomography angiography," Retina **35**, 2163–2180 (2015).
13. K. V. Vienola, B. Braaf, C. K. Sheehy, Q. Yang, P. Tiruveedhula, D. W. Arathorn, J. F. de Boer, and A. Roorda, "Real-time eye motion compensation for OCT imaging with tracking SLO," Biomed. Opt. Express **3**, 2950–2963 (2012).
14. T. Klein, W. Wieser, L. Reznicek, A. Neubauer, A. Kampik, and R. Huber, "Multi-MHz retinal OCT," Biomed. Opt. Express **4**, 1890–1908 (2013).
15. J. P. Kolb, W. Draxinger, J. Klee, T. Pfeiffer, M. Eibl, T. Klein, W. Wieser, and R. Huber, "Live video rate volumetric OCT imaging of the retina with multi-MHz A-scan rates," PLoS ONE **14**, e0213144 (2019).
16. J. P. Kolb, T. Klein, C. L. Kufner, W. Wieser, A. S. Neubauer, and R. Huber, "Ultra-widefield retinal MHz-OCT imaging with up to 100 degrees viewing angle," Biomed. Opt. Express **6**, 1534–1552 (2015).
17. M. Siddiqui, A. S. Nam, S. Tozburun, N. Lippok, C. Blatter, and B. J. Vakoc, "High-speed optical coherence tomography by circular interferometric ranging," Nat. Photonics **12**, 111–116 (2018).
18. I. Grulkowski, J. J. Liu, B. Potsaid, V. Jayaraman, C. D. Lu, J. Jiang, A. E. Cable, J. S. Duker, and J. G. Fujimoto, "Retinal, anterior segment and full eye imaging using ultrahigh speed swept source OCT with vertical-cavity surface emitting lasers," Biomed. Opt. Express **3**, 2733–2751 (2012).
19. D. J. Fechtig, B. Grajciar, T. Schmoll, C. Blatter, R. M. Werkmeister, W. Drexler, and R. A. Leitgeb, "Line-field parallel swept source MHz OCT for structural and functional retinal imaging," Biomed. Opt. Express **6**, 716–735 (2015).
20. S. K. Dubey, T. Anna, C. Shakher, and D. S. Mehta, "Fingerprint detection using full-field swept-source optical coherence tomography," Appl. Phys. Lett. **91**, 181106 (2007).
21. M. A. Choma, M. V. Sarunic, C. Yang, and J. A. Izatt, "Sensitivity advantage of swept source and Fourier domain optical coherence tomography," Opt. Express **11**, 2183–2189 (2003).
22. C. Zhou, A. Alex, J. Rasakanthan, and Y. Ma, "Space-division multiplexing optical coherence tomography," Opt. Express **21**, 19219–19227 (2013).
23. B. Potsaid, V. Jayaraman, J. G. Fujimoto, J. Jiang, P. J. S. Heim, and A. E. Cable, "MEMS tunable VCSEL light source for ultrahigh speed 60kHz–1MHz axial scan rate and long range centimeter class OCT imaging," Proc. SPIE **8213**, 82130M (2012).
24. B. A. Standish, K. K. C. Lee, A. Mariampillai, N. R. Munce, M. K. K. Leung, V. X. D. Yang, and I. A. Vitkin, "In vivo endoscopic multi-beam optical coherence tomography," Phys. Med. Biol. **55**, 615–622 (2010).
25. R. Haindl, W. Trasischker, A. Wartak, B. Baumann, M. Pircher, and C. K. Hitzenberger, "Total retinal blood flow measurement by three beam Doppler optical coherence tomography," Biomed. Opt. Express **7**, 287–301 (2016).
26. S. Zotter, M. Pircher, T. Torzicky, M. Bonesi, E. Götzinger, R. A. Leitgeb, and C. K. Hitzenberger, "Visualization of microvasculature by dual-beam phase-resolved Doppler optical coherence tomography," Opt. Express **19**, 1217–1227 (2011).
27. N. Suehira, S. Ooto, M. Hangai, K. Matsumoto, N. Tomatsu, T. Yuasa, K. Yamada, and N. Yoshimura, "Three-beam spectral-domain optical coherence tomography for retinal imaging," J. Biomed. Opt. **17**, 106001 (2012).
28. H. Y. Lee, H. Sudkamp, T. Marvdashti, and A. K. Ellerbee, "Interleaved optical coherence tomography," Opt. Express **21**, 26542–26556 (2013).
29. Y. Huang, M. Badar, A. Nitkowski, A. Weinroth, N. Tansu, and C. Zhou, "Wide-field high-speed space-division multiplexing optical coherence tomography using an integrated photonic device," Biomed. Opt. Express **8**, 3856–3867 (2017).
30. R. K. Manapuram, V. G. R. Manne, and K. V. Larin, "Development of phase-stabilized swept-source OCT for the ultrasensitive quantification of microbubbles," Laser Phys. **18**, 1080–1086 (2008).
31. A. F. Fercher, C. K. Hitzenberger, M. Sticker, R. Zawadzki, B. Karamata, and T. Lasser, "Numerical dispersion compensation for partial coherence interferometry and optical coherence tomography," Opt. Express **9**, 610–615 (2001).
32. Laser Institute of America, "American national standard for safe use of lasers in health care," ANSI Z136.3-2018 (2018).
33. J. Voke, "Radiation effects on the eye: Part 3b—Ocular effects of ultraviolet radiation," *Optometry Today* (July 30, 1999), 37–40.
34. M. Guizar-Sicairos, S. T. Thurman, and J. R. Fienup, "Efficient subpixel image registration algorithms," Opt. Lett. **33**, 156–158 (2008).
35. S. J. Chiu, X. T. Li, P. Nicholas, C. A. Toth, J. A. Izatt, and S. Farsiu, "Automatic segmentation of seven retinal layers in SDOCT images congruent with expert manual segmentation," Opt. Express **18**, 19413–19428 (2010).
36. R. F. Spaide, J. M. Klancnik, Jr., and M. J. Cooney, "Retinal vascular layers in macular telangiectasia type 2 imaged by optical coherence tomographic angiography," JAMA Ophthalmol. **133**, 66–73 (2015).